

Automatic calibration of powder diffraction experiments using two-dimensional detectors

P. Rajiv, B. Hinrichsen, R. Dinnebier, and M. Jansen

Max Planck Institute for Solid State Research, Heisenbergstraße 1, 70569 Stuttgart, Germany

M. Joswig

Institute for Geophysics, Stuttgart University, Azenbergstraße 16, 70174 Stuttgart, Germany

(Received 4 August 2006; accepted 12 January 2007)

Calibration of powder diffraction experiments using area detectors is essential to extract high quality one-dimensional powder diffraction pattern. Precise calibration necessitates a sensible characterization of the Debye-Scherrer rings formed on the detector plane. An algorithm, designed and developed to automate this process, is described in this paper. All the parameters required for an experimental calibration are extracted using robust pattern recognition techniques. Several image preprocessing methods are employed, reducing the computational cost but retaining high signal quality. A modified version of a one-dimensional Hough transformation is used to determine the final parameters of the ellipses. After extraction, the parameters are optimized using nonlinear least squares fit. The presented algorithm is insensitive to image artefacts and was successfully applied to a large number of calibration images. The performance of the algorithm is demonstrated by the comparison of results obtained from the presented automatic calibration method and an existing manual method. © 2007 International Centre for Diffraction Data. [DOI: 10.1154/1.2486434]

Key words: calibration, ellipse detection, Hough transformation, powder diffraction, area detectors

I. INTRODUCTION

Calibration of diffraction experiments using 2D detectors like image plates and CCD cameras is fundamental to modern powder diffraction. It is crucial in any powder diffraction experiment to obtain reliable angular and intensity data of the diffracting sample. Accuracy of the angular data is generally challenged by the nonorthogonality of the detector with respect to the primary beam axis. High accuracy can only be achieved by the extraction of detector alignment contained in the diffraction patterns.

A well defined diffraction pattern with recognizable shapes is the basic requirement for the accurate extraction and characterization of this information. These requirements are not easily met by all samples because of the folding of micro-structural properties with instrumental contributions. Appropriate calibration standards (LaB₆, SiO₂, and CeO₂) (see https://srms.nist.gov/tables/view_table.cfm?table=209-1.htm) are nearly free of strain and size effects.

The purpose of calibration is to obtain reliable angular data for subsequent measurements of samples not suited for calibration. Successful calibration also avoids peak broadening and irregular peak shapes in the integrated ID intensity versus diffraction angle $I(2\Theta)$ data (Wunschel, 2003), observed for incorrectly calibrated images.

An early method to perform experimental calibration was developed by Hammersley *et al.* (1996). In his method, calibration is done from the parameters of the ellipses selected manually by the user. To our knowledge, Fisker *et al.* (1998) were the first to use the Hough transformation for the automatic extraction of ellipses from powder diffraction patterns. Recently, Cervellino *et al.* (2006) developed a different procedure for calibration using the method of simulated annealing and Hankel Lanczos singular value decomposition for ellipse extraction.

In this paper, we present an algorithm that performs automatic calibration with the aid of modern pattern recognition techniques. Several image reduction methods, along with a one-dimensional Hough transformation (Hough, 1962), are employed to determine the parameters of the ellipses. The layered design of coarse-grain adjustment and subsequent high-resolution fine tuning in the presented algorithm was inspired from a similar approach in medical image processing where X-ray images of chest were automatically corrected from the attenuation of rib bone structures (Schreckenber and Joswig, 1993).

A. Characterization of detector alignment

Diffracted radiation from a powder sample is emitted as a set of Debye-Scherrer cones (Pecharsky and Zavalij, 2003) with opening angles proportional to the lattice spacing d_{hkl} of the sample:

$$4\Theta = 4 \arcsin\left(\frac{\lambda}{2d_{hkl}}\right), \quad (1)$$

where 2Θ is the diffraction angle in detector plane, λ is wavelength of the incident radiation, and hkl is indices of reflection.

When these cones are projected onto a 2D detector they produce a pattern of concentric rings. Diffraction rings produced by a standard sample have continuous contours with well defined edges. Credible information about detector alignment can be extracted from such images.

Debye-Scherrer cones and the detector plane together constitute a conic section. In general a conic section is defined as the shape formed at the intersection of a cone and a plane (shown in Figure 1). The shape formed depends upon the 3D spatial orientation of the intersecting plane. Shapes

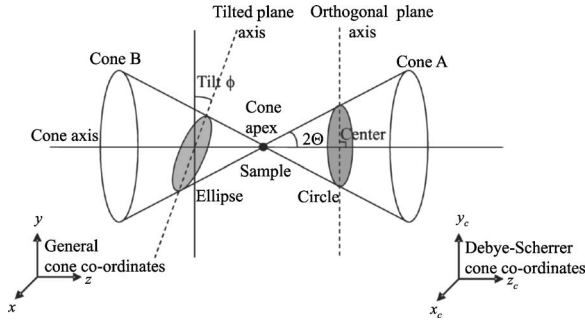


Figure 1. The conic section: The two conics formed at the intersection of a cone and a plane. A circle (cone A) and an ellipse (cone B) are formed resulting from the intersection of a normal and tilted plane, respectively.

described by the bases of two cones on an intersecting plane are shown in Figure 1. A circle is formed as a result of the intersection of cone A with an orthogonal plane, and an ellipse is formed as a result of the intersection of cone B with a tilted plane. For these two shapes the tilt angle range is $0^\circ < \text{tilt} < 90^\circ$.

The equation of the cone that describes a conic section is

$$x^2 + y^2 = (z \tan 2\Theta)^2 \quad (2)$$

where (x, y, z) are the coordinate axes of cones (Figure 1), 4Θ is opening angle of the cone, and z is length of the cone axis.

If the slope of the intersecting plane is $m (m = \tan \phi)$, then the general equation of the shape described by the cone is given by

$$x^2 \left(\frac{1}{(\tan 2\Theta)^2} - m^2 \right) + \frac{y^2}{(\tan 2\Theta)^2} + 2mcx - c^2 = 0, \quad (3)$$

where c is y -intercept of the intersecting plane and ϕ is the angle between the normal vector of the plane and the cone axis.

Depending on the slope m , the general Eq. (3) reduces to the equation of the particular shape described.

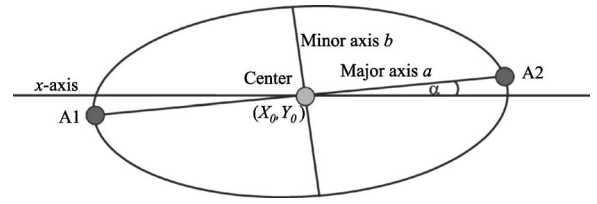


Figure 2. Ellipse: An ellipse and its parameters in 5-D parameter space (orientation or rotation α with respect to the x -axis). A1 and A2 are vertices of major axis.

A similar interpretation can be made for the intersection of Debye-Scherrer cones with a detector plane. The equation of the Debye-Scherrer cone (Hammersley *et al.*, 1996) that describes the powder patterns on the detector plane is

$$x_c^2 + y_c^2 = [(D - z_c) \tan 2\Theta]^2, \quad (4)$$

where (x_c, y_c, z_c) correspond to the coordinate frame of the cone (Figure 1), 2Θ is the diffraction angle of the sample, and D is sample to detector distance.

The diffraction pattern described on the detector plane is given by Eq. (3). If the slope m in Eq. (3) becomes zero, then a set of concentric circles is formed on the orthogonal detector plane.

Experimentally, it is not possible to align the detector exactly orthogonal to the primary beam (Hinrichsen *et al.*, 2006; Hammersley *et al.*, 1996). For a detector tilt ϕ such that $(2\Theta + \phi) < \pi/2$, (3) reduces to the equation (Cervellino *et al.*, 2006) of the ellipse:

$$\frac{x^2}{a^2} + \frac{y^2}{b^2} = 1, \quad (5)$$

where a and b are the major axis and minor axis of the ellipse (Figure 2).

The diffraction angle 2Θ of the sample (Hammersley *et al.*, 1996) is given by

$$2\Theta = \arctan \left(\sqrt{\frac{\cos^2(\phi)(x_d \cos(\alpha) + y_d \sin(\alpha))^2 + (y_d \cos(\alpha) - x_d \sin(\alpha))^2}{(D + \sin(\phi)(x_d \cos(\alpha) + y_d \sin(\alpha)))^2}} \right), \quad (6)$$

where α is rotation of the detector plane and x_d and y_d are the detector coordinates (Hammersley *et al.*, 1996) relative to the beam center:

$$\begin{aligned} x_d &= x - X_0, \\ y_d &= y - Y_0. \end{aligned} \quad (7)$$

The detector to primary beam nonorthogonality causes the diffraction cones to describe a set of confocal ellipses (shown in Figure 3). Accurate detection and refinement of

the parameters describing these ellipses are essential to quantify the detector alignment. Alignment information so extracted is used for a precise calibration of the experiment and to obtain reliable angular data for subsequent diffraction images.

Detection and refinement of parameters from images, in general, are cumbersome and very time consuming (Bennett *et al.*, 1999; Hinrichsen *et al.*, 2006) operations that involve subjective manual interaction (Hinrichsen *et al.*, 2006). In our method we use robust pattern recognition techniques for the automatic extraction and refinement of the ellipse parameters. This method involves no mathematical complexity and exhibits good overall efficiency.

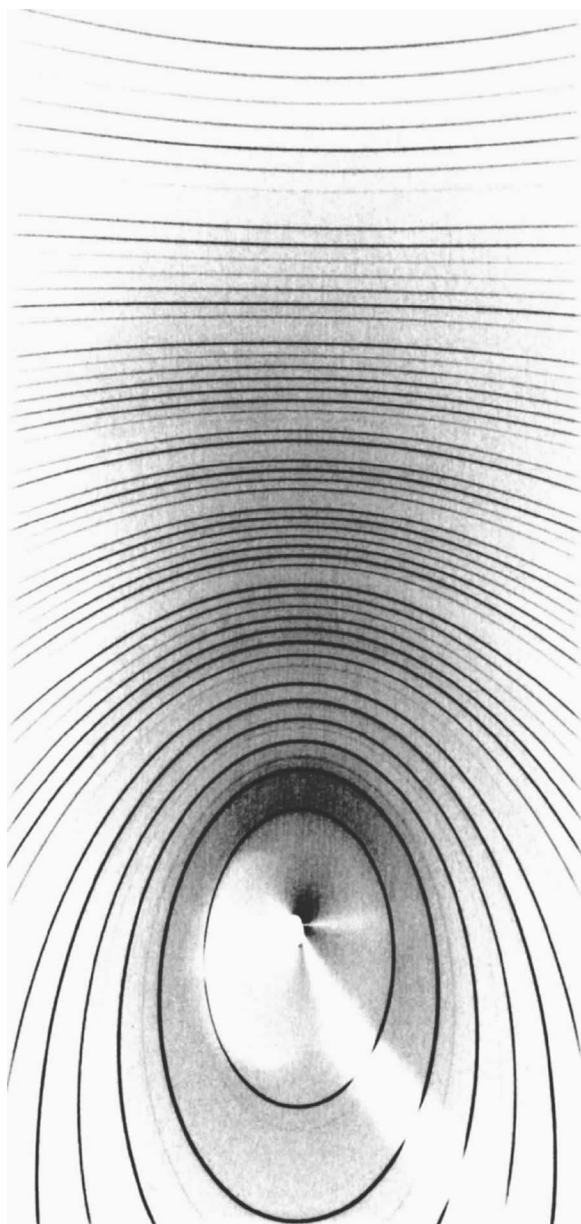


Figure 3. Powder pattern: A pattern of confocal ellipses formed resulting from the nonorthogonality of the detector (large tilt) (Norby, 1997).

B. Ellipse detection techniques

A general ellipse is described by five parameters. The widely used experimental description contains the center coordinates (X_0, Y_0), the spatial orientation or the rotation (α), the major axis (a), and the minor axis (b) (Figure 2).

Detecting all the parameters simultaneously using a single algorithm is very impractical (Lei and Wong, 1999). The complexity of the problem can be reduced by decomposing the process (Chellali and Fremont, 2003) into several simpler stages as shown in Figure 4.

A center detection algorithm based on the mirror symmetry of the intensity along vertical and horizontal grid lines is applied. The center is determined from the intersection of the two lines fitted to the point of symmetry using the method of least absolute deviation. This algorithm is robust against the possible outliers.

Several image preprocessing techniques, including im-

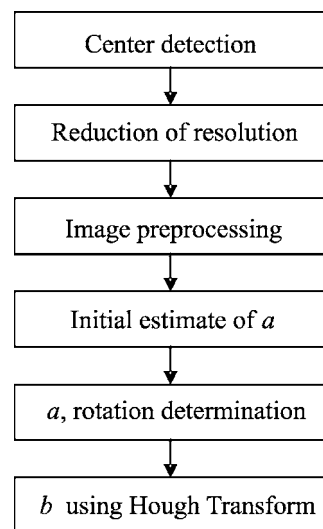


Figure 4. The ellipse detection algorithm: The complete process is decomposed into several modules for simplicity.

age depth reduction and robust background subtraction, are performed to ensure a good signal extraction. Data reduction is performed after the center determination to reduce computational memory costs (Feng and Fainman, 1992).

The major axis is determined with pairs of edge pixels using a Hough based approach without contour evaluation (Lei and Wong, 1999). Initial estimates of the axis lengths are determined using a radial scan of the image. Detected initial estimates are used to constrain the major axis length filtering out spurious pixels not belonging to the required global ellipse space.

Hough transformation (Hough, 1962), a global method to detect analytical shapes in digital images, is used to determine the minor axis of the ellipse. Using the Hough transform for single parameter extraction is advantageous for the accuracy of estimation of the parameter (Lei and Wong, 1999). All the ellipses are detected iteratively, and the detected ellipses are removed from the image immediately after recognition. Processing time is thereby reduced for every detected ellipse.

After the determination of all parameters, the major and minor axis lengths are expressed in the form of the tilt. Experimentally, tilt is a measure of deviation of orthogonality of the detector.

Lattice spacings of the sample are (Pecharsky and Zavalij, 2003) calculated using Eq. (1). They are used to optimize the detected parameters with an algorithm based on Levenberg-Marquardt nonlinear least squares fit (William *et al.*, 2002).

II. CENTER DETECTION

A. Grid symmetry

The center of the ellipses is determined using the mirror symmetry of grid lines drawn on the image. Equally spaced vertical and horizontal grid lines are as shown in Figure 5.

The center detection algorithm is based on the intersection of two lines that lie on mutually perpendicular mirror planes of the ellipses. Each line (two intersecting lines in

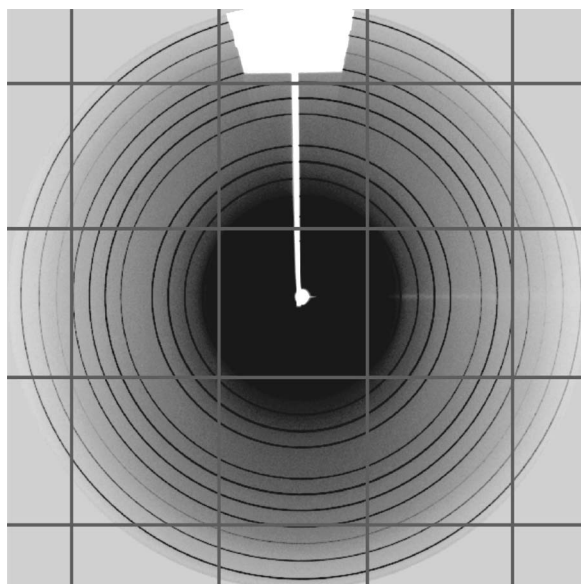


Figure 5. Center detection grids: The horizontal and vertical lines are the center grids on the 2-D powder diffraction pattern of LaB_6 .

Figure 8) is constructed from a set of points belonging to different parallel grid lines. We call these points “mirror points.” A mirror point divides a grid profile into two symmetric and super-imposable mirror halves.

The intensity profile of one of the center grids is shown in Figure 6. Peaks in this profile represent the edge pixels that constitute the ellipses in the image. These peaks are spaced symmetrically on either side of the mirror plane passing through the grid.

Mirror points for this grid profile are calculated by finding the absolute difference in intensities between left and right parts of the profile. A routine iteratively folds the grid histogram along a pixel position and calculates the absolute differences between the overlapping parts. All differences are stored in a second histogram, the abscissa values being the pixel position of the fold (Figure 7).

The primary minimum in the difference array (the deepest minimum in Figure 7) is the position at which the maximum overlap of peaks on right and left sides occurs. Using the median of the difference to filter out the left and right slopes, this position is calculated. The index corresponding

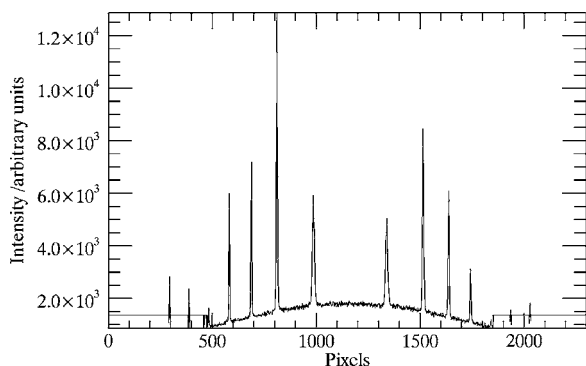


Figure 6. Grid intensity: Profile along a grid line of Figure 5. The peaks correspond to the ellipses (the zero and lower intensities are replaced by the grid median for computational simplicity).

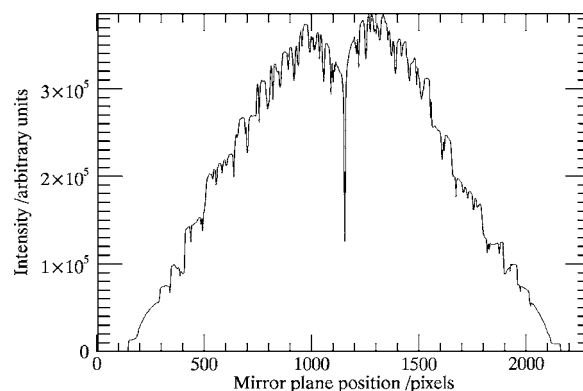


Figure 7. Difference array: The difference histogram of a grid profile with many minima and the primary minimum on the mirror plane.

to this minimum position is the mirror point for that grid. Many mirror points are obtained for a set of grids along two directions.

The number of grid lines used is set to a default value of 10, as most of the tested images were successfully analyzed with this value. Image artefacts are very well compensated and a quicker computation of the parameters is achieved by this relatively small value.

We obtain two sets of mirror points, one for the vertical grids and one for the horizontal grids (Figure 8). Two lines, one for the vertical and one for the horizontal set of points, are fitted using the method of least absolute deviation. The point of intersection of these lines gives the center of the ellipse. This fitting method is robust and outlier insensitive, offsetting the uncertainties caused by the beam stop shadow and partial image occlusion.

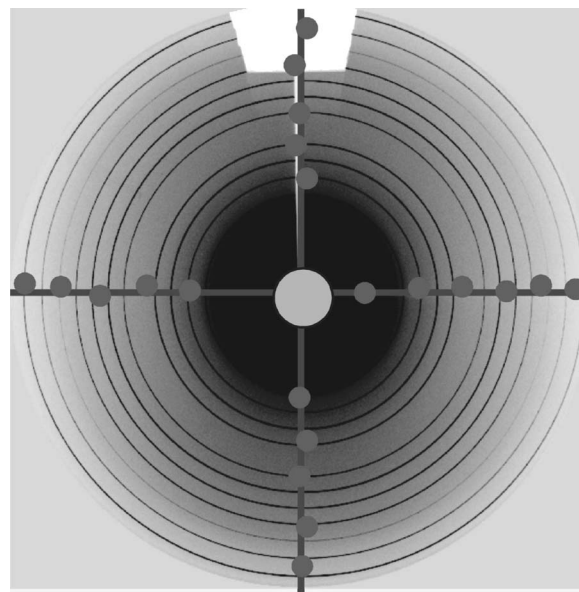


Figure 8. Center finding: The dots along the lines are the mirror points determined from the grids. The lines are fitted to these points by the method of least absolute deviation. The intersection of lines (larger circle near the image center) represents the center of the image.

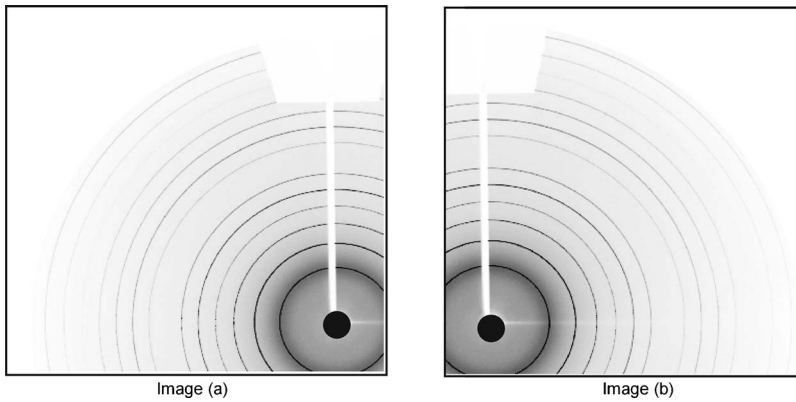


Figure 9. Test image of LaB₆: Two test images (a) and (b) with the modified center positions (indicated by dark circles).

B. Improvements in the algorithm

An analysis of various images has shown that noisy pixels present in image boundaries can affect the symmetry of the center detection grids passing through them. Before proceeding to find the center, the image boundary is checked for these noisy pixels. These pixels have nonuniform intensities and are distributed randomly along a line close to the image boundary. Indices of all the pixels along this line with non-zero intensities are stored in an array. A linear fit to this array results in a large mean absolute deviation because of the randomness of the indices. Using the magnitude of the deviation, the spurious boundary pixels can be separated and removed from the image.

The primary minimum in the difference profile (Figure 7) is searched within an intensity limit set by the median of the difference array. The median of a grid with a large number of zero intensity pixels is not suitable to define this limit. To overcome this problem, zero and lower intensity pixels in the grid histogram are replaced by the median (Figure 6).

Depending on the image noise, the fluctuations of data points in the difference array (Figure 7) may vary. In extreme cases, a large number of identical primary minima appear in the difference histogram profile. The grid histogram is smoothed using an algorithm based on box-car averaging (William *et al.*, 2002) minimizing the fluctuations in the difference array.

C. Robustness of the algorithm

The center detection algorithm is robust against high intensity spikes (Hinrichsen *et al.*, 2006) in images lacking good statistical averaging (like images of FeSbO₄). Outliers, found in such images, shift the mirror point randomly. Small uncertainties caused by the shift are compensated by the “outlier insensitive” least absolute deviation fit.

TABLE I. Robustness of the center detection algorithm: The detected centers of two test images [Image (a) and Image (b)] are compared with expected centers.

Images	Detected center (x, y) in pixels	Expected center (x, y) in pixels
Image (a)	(293.354, 77.280)	(304.863, 49.017)
Image (b)	(38.142, 71.244)	(35.137, 49.062)

This algorithm has proven to be robust against the position of the ellipses with respect to the image center. The original image of dimension (x, y) is cropped along two intermediate lengths x_i and y_i to get an image of new dimension (x_i, y_i). The beam center coordinates for this image appear to be shifted far from the geometric center of the image. Two images cropped along two different sets of x and y distances are shown in Figure 9.

The center detection algorithm is tested on the two images in Figure 9. The detected centers of these images are compared to their expected centers in Table I. The expected centers are approximated from the difference between the center of the original image and the dimension of the cropped image:

Dimension of image (a) (x_i, y_i) = (350, 350) pixels,

Dimension of image (b) (x_j, y_j) = (340, 350) pixels,

Center of original image
(X_0, Y_0) = (304.863, 300.983) pixels.

The large aberrations in detected y coordinates in Table I are the result of the higher influence of the image artefacts, in

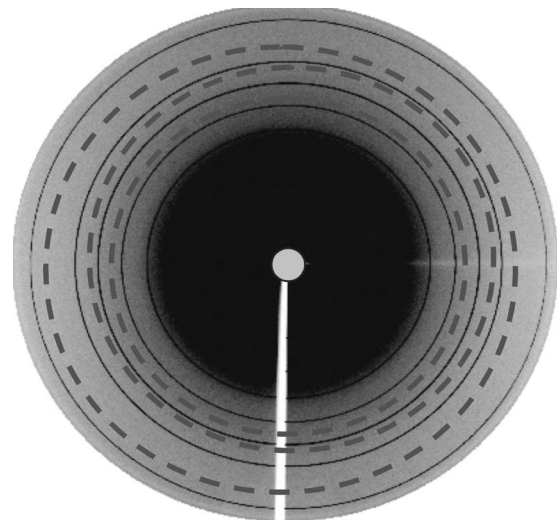


Figure 10. Segmentation: The image is divided into segments of different radii along the detected center. The segments are denoted by dotted circles and detected center by a small circle.

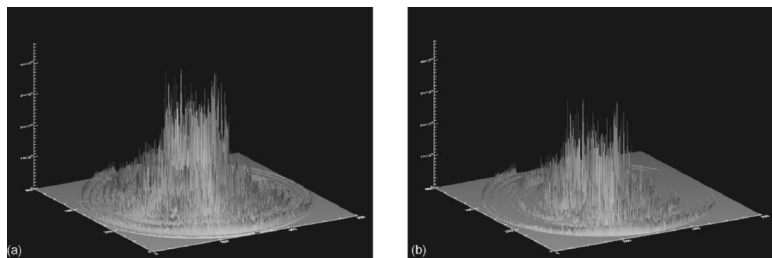


Figure 11. Background subtraction: 3-D intensity distribution of the image. The images with high background (a) and subtracted background (b) are compared.

this case the shadow of the primary beam stop shadow. Irrespective of the geometric positions of the ellipses, the center is detected by the algorithm. A requirement of this algorithm is that the center of the ellipses has to be on the image.

III. IMAGE PREPROCESSING

A. Reduction of resolution

The spatial resolution of powder diffraction images is normally on the order of a few thousand pixels squared. Manipulation of such a huge amount of data costs a lot of time and memory. The computational complexity of an image of resolution $N \times N$ is $(N \times N)^4$ (Feng and Fainman, 1992). Moreover, the implementation of a Hough transformation requires an accumulator memory in the order of approximately N^4 . The original image resolution is reduced by a factor of 4 to ensure efficient computations. The reduction factor 4 has proven to be sufficient for our data to retain a high accuracy of the estimated parameters.

B. Background reduction and thresholding

Background reduction and thresholding are important preprocessing steps in preparing the image for a Hough transformation. Diffraction images are surrounded by cloudy background mainly originating from the scattering of X-rays by air molecules. Background intensity of X-ray images is high near the incident beam and decreases gradually towards higher 2θ angles (Fisker *et al.*, 1998). Subtracting the background for such images with nonuniform intensity distribution is crucial.

The entire image is divided into segments of different radii. The average intensity of each segment (Figure 10) differs from the others.

Background reduction is accomplished by subtracting twice the median from all the pixels inside a segment. Three-dimensional view of the image before and after subtraction is shown in Figure 11.

After background subtraction, the image is thresholded into a binary image. The threshold is applied by setting the pixels of high intensity to 1 and the rest to 0. For an efficient Hough transformation (Fung *et al.*, 1996), this conversion is absolutely necessary.

It is extremely important for images to be subjected to background reduction in order to choose a single optimal threshold value for the entire image. Binary images obtained without background reduction and with background reduction are compared in Figure 12.

Near the center of the binary image obtained without background subtraction a lot of noise has accumulated [Figure 12(a)]. With this noise the resolution and extraction of inner ellipses become extremely difficult. The binary image in Figure 12(b) has been obtained after background subtraction. It has sharp resolvable edges, which are imperative for an effective Hough transform.

C. Optimal segmentation

The background subtraction routine is designed to work for all magnitudes of ellipse eccentricities. Background subtraction is accomplished by the subtraction of twice the median in the segmented image. The radii of the segments are carefully chosen so that the first segment encloses the innermost ellipse, which is most influenced by the image background.

For highly eccentric ellipses good segmentation provides uniform background subtraction. Images obtained without a sensible segmentation (Figure 13) contain background near the inner ellipse and are unsuitable for further processing.

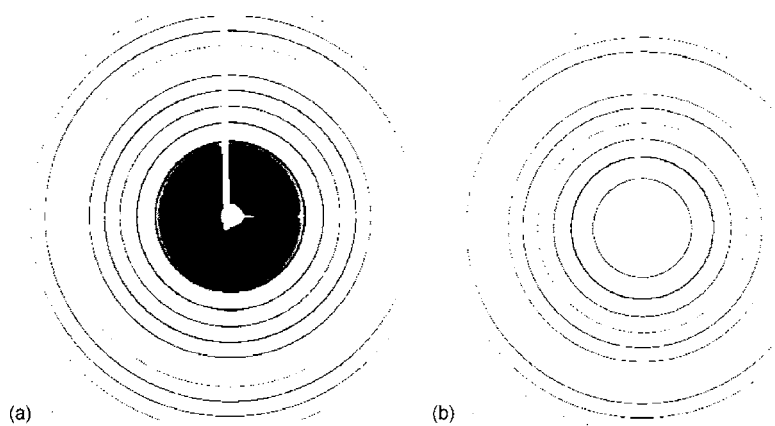


Figure 12. Threshold image: Bit scaled images before background subtraction (a) and after background subtraction (b).

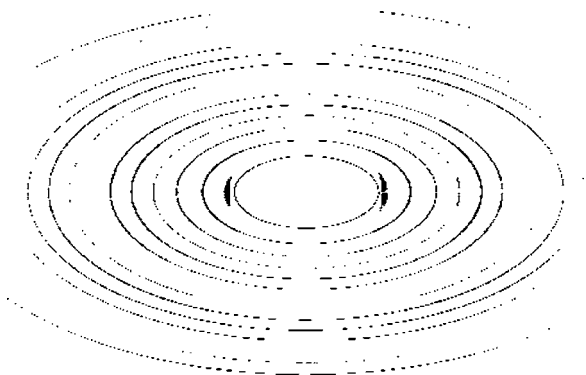


Figure 13. Poor segmentation: The binary image obtained because of insensible segmentation radii. The inner most ellipse is surrounded by background because of incorrect segmentation radii.

To choose proper segmentation radii, the estimate of major axis length of the innermost ellipse is found first. The binary image obtained after a 30% threshold is used for this purpose. About 105% of the major axis length is set as the radius of the first segment. A sensible first-segment radius is sufficient for an efficient background subtraction. This method of background reduction and threshold works for nearly circular ellipses as well as for highly eccentric ellipses.

D. Optimal thresholding

The best values for the background subtraction and thresholding are determined from the optimal balance between occlusion and resolution of ellipses. The subtraction of twice the median intensity provides substantial background reduction and good signal extraction for a wide range of data.

Many suitable threshold values have been tested. An image obtained using a threshold of 8% is shown in Figure 14(a). Inner ellipses in Figure 14(a) are still influenced by the background and they remain badly resolved. A threshold of 12% causes strong occlusion of outer ellipses [Figure 14(b)]. An optimal threshold of 10% typically produces ellipses with continuous edges and a good resolution (Figure 15).

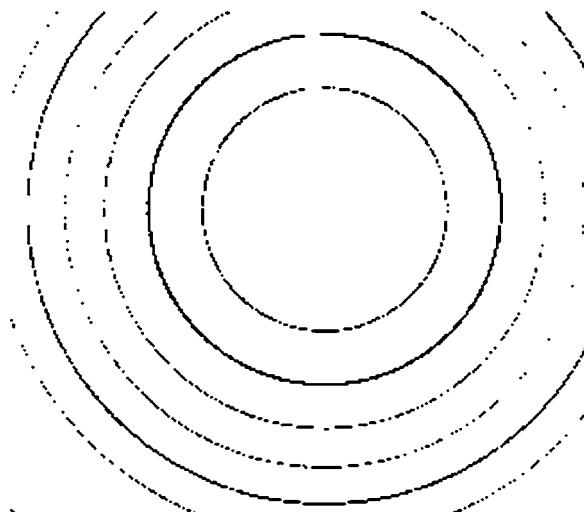


Figure 15. Optimal bit-scaled image: Image obtained after an optimal threshold of 10%. The ellipses have good resolution and continuous contours.

E. Quality check of estimated center

The quality of the preprocessed image can be used to assess the accuracy of center detected by the “center detection algorithm.”

A background subtraction is performed on the image, which is segmented around the detected center. An accurately determined center always results in symmetric segmentation of the image and a uniform background subtraction. Resolvable ellipses with uniform contour thickness are produced if the center used for segmentation is precise. A comparison is made between the image preprocessed with the detected center and an image preprocessed with a modified center (Figure 16).

Inner ellipses in Figure 16(a) are completely resolved and their edges have uniform thickness. The x coordinate of the detected center is now modified and the modified coordinates are used for the segmentation and background subtraction. The binary image obtained using the modified center is shown in Figure 16(b).

In Figure 16(b) the innermost ellipse (indicated by the arrow) is not very well resolved and it has nonuniform contour thickness. Nonuniformity of the contour arises only if

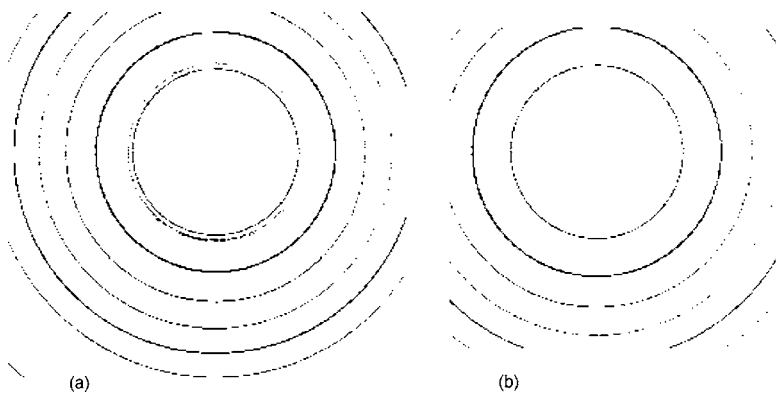


Figure 14. Optimal threshold: The images obtained after 12% thresholding (a) with partially occluded outer ellipses. The images obtained after 8% thresholding with unresolved inner ellipses (b).

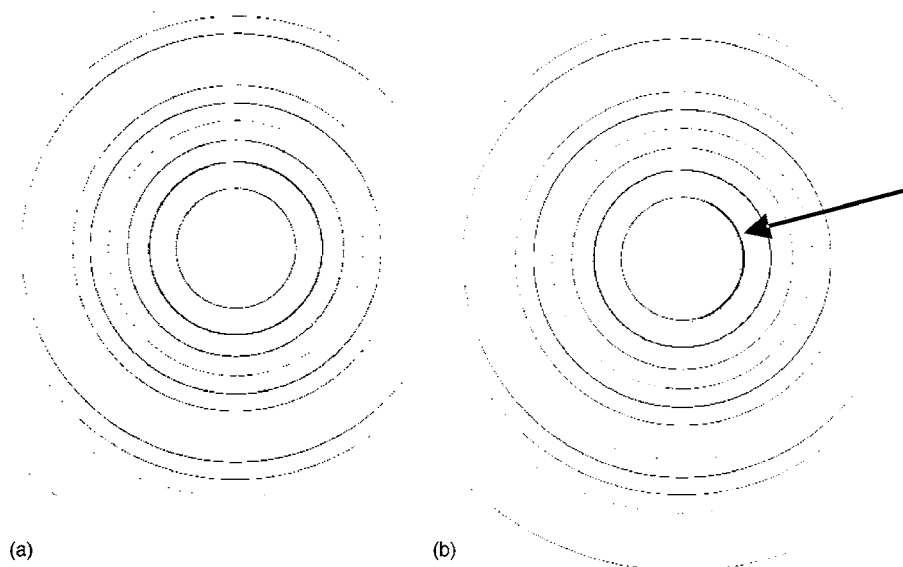


Figure 16. Binary images obtained from detected center (a) and modified center (b): In the binary image obtained using the detected center (a) the inner ellipses are well resolved with uniform contour thickness. In the image obtained from the modified center (b), asymmetry in contours of inner ellipses is seen (indicated by the arrow).

the segmentation was made using an inaccurate center. Similar results are obtained if the y coordinate of the center is modified.

IV. ESTIMATION OF MAJOR AXIS

A. Initial estimate of major axis length

An initial estimate of major axis length is made to put geometric restraint on the global search of the major axis length. Spurious pixels unlikely to be of an ellipse can be filtered out using this estimate. Time and space requirements for the search of the major axis length are reduced by this constraint.

Radial distances of the ellipses are calculated using a complete azimuth scan of the binary image. Many calculated distances are separated and matched with the appropriate ellipses using the ratio of the ellipse radii. Correctly matched

distances are stored in one array per ellipse. The maximum value in the array gives the initial estimate of major-axis length for the ellipse.

B. Azimuthal scan of image

Radial distances of the pixels scattered in a certain azimuth wedge (shown in Figure 17) are interpolated to get the intensity profile along a line.

An interpolated (William *et al.*, 2002) distance-intensity profile for one of the radial lines is shown in Figure 18.

Peaks positions in the histogram represent the distances of ellipses from the center. Because of large scattering of the ellipse pixels in an azimuth wedge, many closely spaced peaks appear on the histogram (Figure 19).

These peaks, representing a single ellipse, will sometimes be incorrectly recognized as a separate ellipse during the histogram scan. To avoid the incorrect recognition of ellipses they must be disregarded.

Multiple histogram peaks are filtered out by constraining their positions with the shortest ratio between neighboring

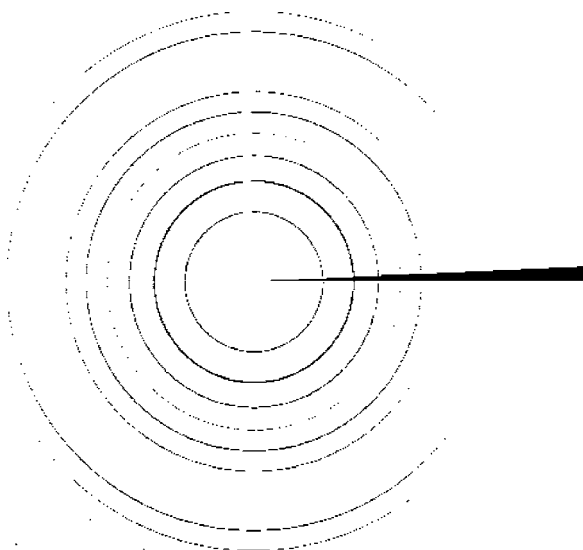


Figure 17. Azimuth scan: The pixels lying within an azimuth wedge of width 2.5° .

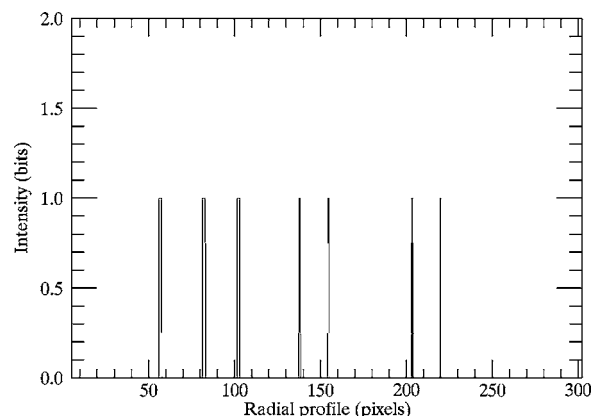


Figure 18. Radial distance and bit intensity: The interpolated array of azimuthal pixels. The peaks in the histogram represent the ellipses.

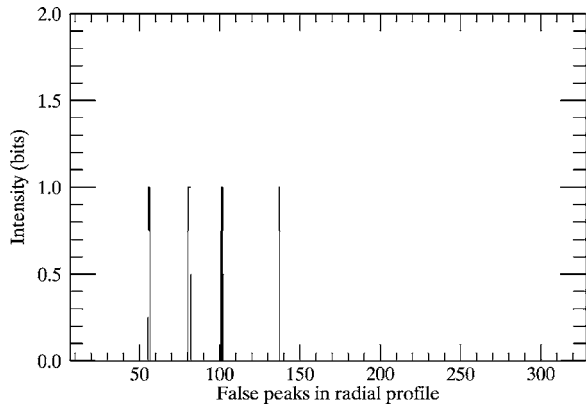


Figure 19. False distance peaks: The closely spaced multiple peaks (near the distance of 100 Pixels) represent a single ellipse in a radial profile.

ellipses. The shortest ratio is determined from the boundary conditions like sample distance, wavelength, and standard lattice spacings of the sample.

Radial profile histograms are scanned to locate the peak positions of the filled bins. The average distances of the ellipses from the center are calculated from the starting and ending locations of filled bins. For better statistics, about 24 radial lines were drawn with the azimuth width set to 2.5. The number of radial lines and the azimuth range are optimized to compensate for the lost data resulting from thresholding.

After a complete scan we have a set of 24 arrays, each corresponding to a radial line.

C. Correctly matched distances

An azimuthal scan is done on the binary image obtained by thresholding the intensity of the original image. Generally the weaker pixels in the original image may not be completely recognized in the binary image. Because of the partial occlusion, some radial distance arrays may not contain the distance information of all the ellipses. In such cases the

TABLE II. Incorrectly matched radial distances: The distances along a row represent different ellipses. The distances along a column represent the radial scan for an ellipse. The distances in **bold** denote the wrongly recognized radii. The radial distance arrays are calculated for the standard sample LaB₆.

Radial distances	Ellipse index								
	1	2	3	4	5	6	7	8	9
1	57.159	82.688	103.187						
2	57.333	82.362	102.970	138.339					
3	57.3190	82.508	103.027	138.264					
4	57.5150	82.466	102.938	120.979	138.380	154.694			
5	57.2523	82.747	103.542	138.219					
6	57.072	82.574	102.963	121.269	138.250	154.851	203.141	219.616	
7	57.298	82.557	103.000	121.211	138.376	154.842	203.126	219.453	
8	57.625	82.545	102.908	121.286	138.341	154.734	203.032	219.352	289.703
9	57.362	82.316	138.367	202.962	219.372	289.437			
10	57.247	82.639	102.923	121.059	138.234	154.816	203.082	219.368	236.024
11	57.212	82.284	102.849	121.019	138.274	154.543	203.068	219.408	289.695
12	57.008	82.234	102.809	120.900	138.163	154.598	203.011	219.318	289.835
13	57.170	81.894	102.725	120.816	137.865	154.475	202.881	219.437	290.044
14	57.010	82.035	102.655	120.766	137.959	154.541	203.061	219.337	
15	56.593	81.9065	102.226	120.630	137.939	154.495	202.796		
16	82.015	102.162	120.445	137.868	154.358				
17	56.492	81.530	102.035	120.094	138.009	154.485			
18	56.281	81.621	102.095	120.465	137.890	154.662	203.018		
19	56.393	81.701	102.241	120.608	137.994				
20	56.216	81.594	101.909	137.931	154.287	203.161			
21	56.408	81.528	102.112	120.541	137.552	154.280	203.273	219.660	
22	56.327	81.694	102.170	120.385	137.744	154.370	203.147	219.712	
23	56.389	81.444	102.301	120.626	137.818	154.611	203.122	219.914	
24	56.657	81.632	102.153	120.557	137.938	154.442	203.225	219.730	290.787
25	138.469	154.509	203.369	219.779					
26	56.539	81.672	102.338	120.884	138.068	154.419	203.169	219.823	
27	56.664	81.778	102.371	120.668	138.105	154.536	203.400	219.976	
28	56.5600	82.163	102.497	120.939	138.030	154.581	203.422		
29	56.946	81.786	102.663	138.030	154.649				
30	56.799	82.027	102.554	120.880	138.076				
31	56.964	82.022	121.038	138.197					
32	57.162.	82.246	138.214						

TABLE III. Matched radial distances: The distances along a row represent different ellipses. The distances along the n th column represent the radial profile of the n th ellipse. Distances corresponding to the poorly occluded ellipses are replaced with zeros. The distances along the 12th row represent the best profile.

Radial distances	Ellipse index								
	1	2	3	4	5	6	7	8	9
1	57.159	82.688	103.187	0.000	0.000	0.000	0.000	0.000	0.000
2	57.333	82.362	102.970	0.000	138.339	0.000	0.000	0.000	0.000
3	57.319	82.508	103.027	0.000	138.264	0.000	0.000	0.000	0.000
4	57.515	82.466	102.938	120.979	138.380	154.694	0.000	0.000	0.000
5	57.252	82.747	103.542	0.0000	138.219	0.000	0.000	0.000	0.000
6	57.072	82.574	102.963	121.269	138.250	154.851	203.141	219.616	0.000
7	57.298	82.557	103.000	121.211	138.376	154.842	203.126	219.453	0.000
8	57.625	82.545	102.908	121.286	138.341	154.734	203.032	219.352	289.703
9	57.362	82.316	0.0000	0.000	138.367	0.000	202.962	219.372	289.437
10	57.247	82.639	102.923	121.059	138.234	154.816	203.082	219.368	236.024
11	57.212	82.284	102.849	121.019	138.274	154.543	203.068	219.408	289.695
12	57.008	82.234	102.809	120.900	138.163	154.598	203.011	219.318	289.835
13	57.170	81.894	102.725	120.816	137.865	154.475	202.881	219.437	290.044
14	57.0101	82.035	102.655	120.766	137.959	154.541	203.061	219.337	0.000
15	56.593	81.906	102.226	120.630	137.939	154.495	202.796	0.000	0.000
16	56.492	81.530	102.035	120.094	138.009	154.485	0.0000	0.000	0.000
17	56.281	81.621	102.095	120.465	137.890	154.662	203.018	0.000	0.000
18	56.393	81.701	102.241	120.608	137.994	0.000	0.000	0.000	0.000
19	56.216	81.594	101.909	0.000	137.931	154.287	203.161	0.000	0.000
20	56.408	81.528	102.112	120.541	137.552	154.280	203.273	219.660	0.000
21	56.327	81.694	102.170	120.385	137.744	154.370	203.147	219.712	0.000
22	56.389	81.444	102.301	120.626	137.818	154.611	203.122	219.914	0.000
23	56.657	81.632	102.153	120.557	137.938	154.442	203.225	219.730	290.787
24	56.539	81.672	102.338	120.884	138.068	154.419	203.169	219.823	0.000
25	56.664	81.778	102.371	120.668	138.105	154.536	203.400	219.976	0.000
26	56.560	82.163	102.497	120.939	138.030	154.581	203.422	0.000	0.000
27	56.946	81.786	102.663	0.000	138.030	154.649	0.000	0.000	0.000
28	56.799	82.027	102.554	120.880	138.076	0.000	0.000	0.000	0.000
29	56.964	82.022	0.000	121.038	138.197	0.000	0.000	0.000	0.000
30	57.162	82.246	0.000	0.000	138.214	0.000	0.000	0.000	0.000

calculated distances would not be correctly matched with the appropriate ellipse index. The array of distances obtained in the radial scan is shown in Table II.

In Table II, the distances along a row represent the histogram peaks (Figure 18) of a radial profile. Distances along the n th column correspond to the radial distances of the n th ellipse for the complete azimuth scan of the image. Column distances for a given ellipse must vary periodically, if there were no partial occlusions. Clearly there is a lack of periodicity in the measured radii (indicated by bold numbers in Table II).

To match the correct radius to the corresponding ellipse index, we choose the best radial profile out of 24 profiles. The best profile contains a maximum number of histogram peaks and also passes through the innermost ellipse. Distance ratios between outer ellipses to the first ellipse for this standard line are calculated. The calculated array is compared with other radii-ratio arrays. Distances are sorted and matched to their respective ellipses using a routine based on the bubble sort method. Distances matched to correct ellipses are listed in Table III.

Distances along the column in Table III (corresponding to the radial scan of the ellipses) show a good periodicity

(illustrated in Figure 20). The maximum of the distance along the n th row gives the initial estimate of the semi-major axis length of the n th ellipse.

Each horizontal line in Figure 20 corresponds to the distance array obtained after the radial scan of an ellipse.

D. Major axis determination

Major axes of the ellipses are determined using a Hough based global algorithm (Chellali and Fremont, 2003). The method assumes a pair of edge pixels (A1 and A2 in Figure 2) to be the vertices of the major axis (Chellali and Fremont, 2003). The distance between them is calculated and constrained using the initial estimate. The midpoint is then calculated for the constrained pixels.

If the calculated mid point of the pixels lies close to the detected center, then the distances between the pixels and their coordinates are stored. Distances and coordinates for all pairs of pixels satisfying these two conditions are stored in an array. The maximum of this array gives the best estimate of major axis length.

Using the coordinates of the major axis (corresponding

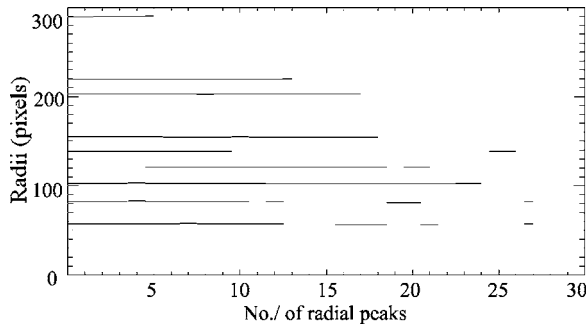


Figure 20. Radial distances of all the ellipses: The radial distances obtained after matching the ellipses with the correct distance arrays.

to A1 and A2 in Figure 2), the orientation (rotation) of the ellipse (Chellali and Fremont, 2003) is calculated from

$$\alpha = \arctan \left(\frac{y_2 - y_1}{x_2 - x_1} \right), \quad (8)$$

where α is the orientation, and (x_1, y_1) and (x_2, y_2) are the coordinates of a pair of pixels.

The major axis lengths of all the ellipses in the image are iteratively calculated and stored. We can also assume the two points A1 and A2 to be the vertices of the minor axis, but it would increase the complexity of the problem (Chellali and Fremont, 2003). The major axis length finder extracts the parameter using pairs of pixels without evaluation of the edge contours. This makes it insensitive to image noise (Lei and Wong, 1999), enabling it to represent the global information of a contour more stably.

We consider only the pairs of pixels within a certain distance range. Very close pixels, which are noise sensitive (Lei and Wong, 1999), are ignored.

V. MINOR AXIS ESTIMATION USING HOUGH TRANSFORMATION

A. Hough transformation

Hough transformation (Hough, 1962) is a global method, used to extract arbitrary shapes from digital images. The method works by the recognition of points in a new transformed space called the parameter space. The transformation is implemented by quantizing the parameter space into finite intervals called the accumulator array. Possible magnitudes of recognized parameters are voted (Dammer *et al.*, 1997) in their corresponding accumulator bin in parameter space. After processing all the edge points in the image, the local maximum in the accumulator array corresponds to the parameter of specified shape.

Generally the Hough transformation works best with images containing clear and descriptive edges. Powder diffraction images obtained after preprocessing contain sharp edges and are well suited for the application of the Hough transformation.

The Hough transformation is robust against the partly occluded ellipses in bit-scaled powder diffraction images.

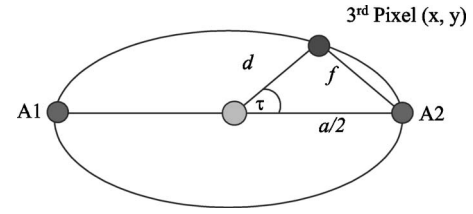


Figure 21. Minor axis length: Third pixel (x, y) in the ellipse is chosen. Its distance d from the center is used to calculate the minor axis.

B. Determination of minor axis of ellipse

After finding the length of the major axis, a third pixel (Figure 21) in the ellipse is chosen and its distance from the center is calculated. We restrict this distance (d) to be less than the semi-major axis length ($a/2$).

The probable length of semi-minor axis is calculated (Chellali and Fremont, 2003) for this pixel using

$$b = \sqrt{\frac{a^2 d^2 \sin^2 \tau}{2(a^2 - d^2 \cos^2 \tau)}}, \quad (9)$$

where $\cos^2 \tau$ is

$$\cos^2 \tau = \left(\frac{a^2 + d^2 - f^2}{2ad} \right)^2 \quad (10)$$

with (τ, d) being the polar coordinates of the assumed pixel and f the distance of this pixel from the nearest major-axis vertex (A1 or A2) (Figure 21).

The accumulator array is incremented for all the pixels satisfying the distance constraint. After processing all the points in the image, the local maximum of the accumulator array gives the semi-minor axis length (Figure 22).

The peaks in Figure 22 represent many possible lengths of the semi-minor axis for a given ellipse. The maximum in the array corresponds to the most probable length of the semi-minor axis.

We only use the Hough transformation to determine the minor axis of ellipses. Only a one-dimensional accumulator array is required for voting. A large amount of memory is saved, as the accumulator array dimension is directly related to the usage of memory (Kanatani and Ohta, 2001).

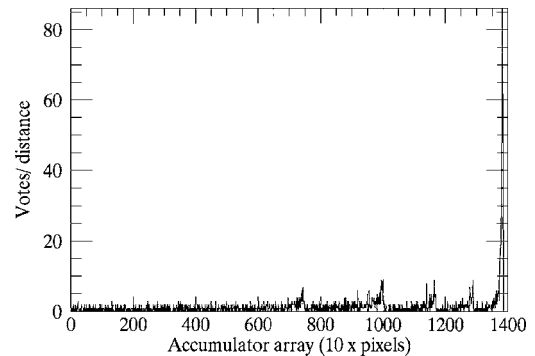


Figure 22. The accumulator array: The quantized 1-D accumulator array used for parameter voting. The maximum peak corresponds to the most probable minor axis length.

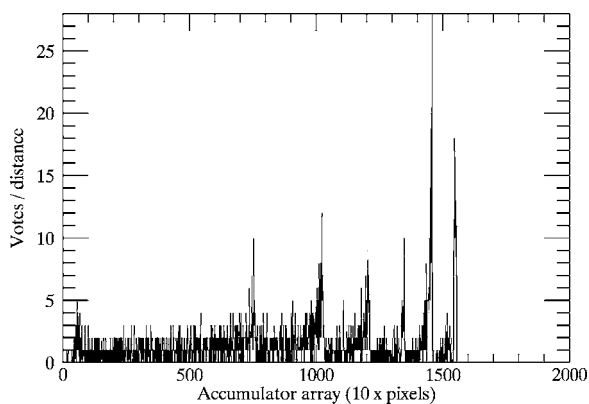


Figure 23. False peaks in accumulator array: The false-maximum peak (at a distance of approximately 1350 pixels) is the length traced for the combination of two inner ellipses.

C. Multiple peaks in accumulator space

The accumulator array corresponding to the semi-minor axis length of an outer ellipse is shown in Figure 23. There are multiple peaks in the accumulator array, each representing a possible minor axis length. Generally they result from the wrong axis lengths traced for an inner ellipse or a combination of two inner ellipses.

Even after a sensible background subtraction and thresholding, X-ray diffraction patterns have high intensities near the beam center. There are fewer pixels in outer ellipses than in inner ones for voting the accumulator array. The influence of inner ellipses is always much greater than the outer ones, which is characterized by many false maxima in the accumulator array. One of them is shown in Figure 23 (the peak lying at the distance of about 1350 pixels between two peaks). The influence of this false minimum will affect the accuracy of the minor axis length.

To eliminate them from the accumulator array, we start the parameter detection for the innermost ellipse first and then proceed outwards. After recognition of the minor axis length of an ellipse, its pixels are removed from the image, and the remaining ellipses in the image are detected iteratively.

A comparison is made between the accumulator array obtained (for the same ellipse) without and with iterative removal of preceding ellipses in Figures 23 and 24. In Figure

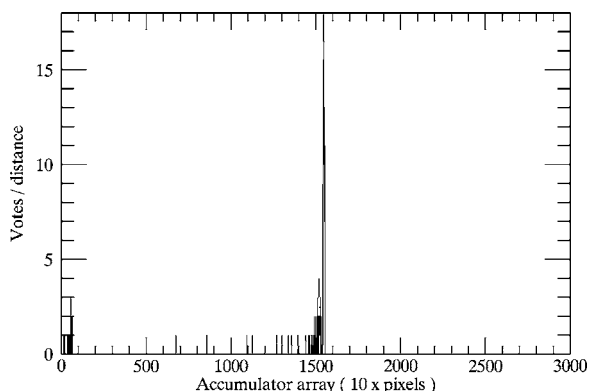


Figure 24. Accumulator array with ellipses removed after detection: A clean accumulator array is obtained without the influence of strong inner ellipses.

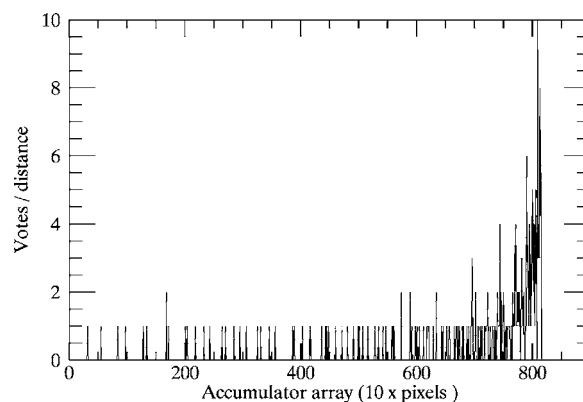


Figure 25. Accuracy of the center in terms of accumulator maxima: Minor axis accumulator array obtained for the center detected from the algorithm. No multiple peaks are present.

24 we find that the accumulator space obtained after the removal of ellipses is clear and not influenced by the dense inner ellipses. Most reliable lengths of minor axes are obtained from such an array. The computational cost for detecting b decreases with every ellipse after the removal of their pixels from the image.

D. Multiple peaks because of inaccurate center

The semi-minor axis lengths are calculated by the voting of ellipse radii (" d " in Figure 21) in respective accumulator bins. Apart from the influence of the dense inner ellipses, all the accumulator arrays have well defined local maximum (one of them is shown in Figure 25). The detected center is used to construct the accumulator array in Figure 25.

To estimate the effect of an inaccuracy, the detected x center coordinate is now slightly shifted by 10 pixels and used to constrain the semi-minor axis lengths. The accumulator array constructed using the modified center contains an extra peak (shown in Figure 26). An extra peak in the accumulator array appears only if the shift is large enough. In other words, the detected center is so precise that the accumulator array obtained using it (Figure 25) is least influenced by multiple peaks.

In less eccentric ellipses like powder diffraction rings, inaccurate center coordinates reduce the number of votes for

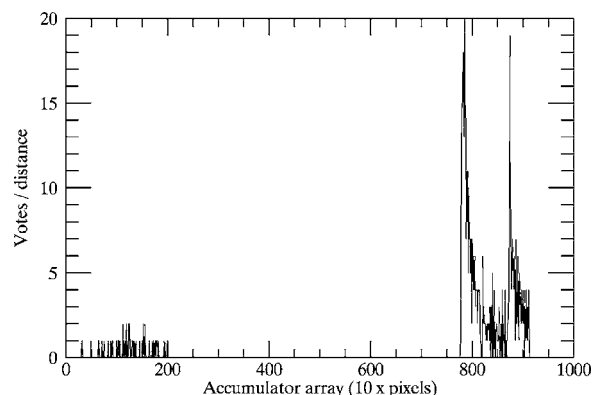


Figure 26. The accumulator array for an inaccurate center: The multiple peaks appear resulting from the inaccuracy in initial center estimation.

TABLE IV. The detected parameters: The parameters detected for a standard sample of LaB_6 are listed. The axes lengths are in pixels and the rotation in degrees.

	Parameters		
	Major-axis length (a) (pixels)	Minor-axis length (b) (pixels)	Rotation (α) (deg)
Ellipses			
1	57.280	57.200	106.222
2	82.756	80.900	4.505
3	103.012	102.600	89.166
4	121.149	120.800	70.219
5	138.600	138.300	73.657
6	155.003	154.500	103.050
7	203.648	203.300	77.090
8	219.920	219.500	73.625
9	290.460	289.800	108.778

the most probable estimate of axis length, producing an extra peak in the accumulator array. The influence of this peak increases with the inaccuracy of the center.

In Figure 26 the heights of the peaks suggest inaccuracy of the detected center. The lack of extra peaks in the accumulator array in Figure 25 implies that the center detected by the algorithm is of high accuracy. It is extremely important to calculate the center with good accuracy as the determination of all other parameters relies on a precise center.

VI. ANALYSIS OF RESULTS AND LEAST SQUARES REFINEMENT

A. Implementation of algorithm

The ellipse detection algorithm is tested on an image of a standard sample LaB_6 . The quality and performance of the algorithm is tested on the precision of the extracted parameters. Original dimensions of the image (2300 pixels squared) are reduced by a considerable factor of 4 to accomplish an optimal threshold and efficient parameter extraction.

An accurate determination of the center is imperative for successful preprocessing and precise detection of other parameters. To gain good center accuracy, the original data is used for the center determination and the detected center is normalized for the reduced dimension. The normalized center coordinates of the reduced image of LaB_6 are $X\text{-Center}=304.862$ (pixels) and $Y\text{-Center}=300.983$ (pixels).

Nine ellipses out of 14 from the reduced, preprocessed image could successfully be extracted by the algorithm. The detected parameters of the ellipses are listed in Table IV.

Table IV lists the parameters of complete and high intensity ellipses. Parameters of the partly occluded ellipses are ignored using a constraint in the eccentricity of the completely defined inner ellipse.

Estimates of axes lengths (a and b) in Table IV are in good agreement with the initial estimates. The accuracy of the extracted parameters is confirmed by the consistency in the order of the ellipse eccentricities.

Rotation of the ellipses (the slope of the major axis) are determined directly from the vertices of major axis [Eq. (8)]. Large scattering of rotations seems to imply a large uncertainty in the estimation of major axis.

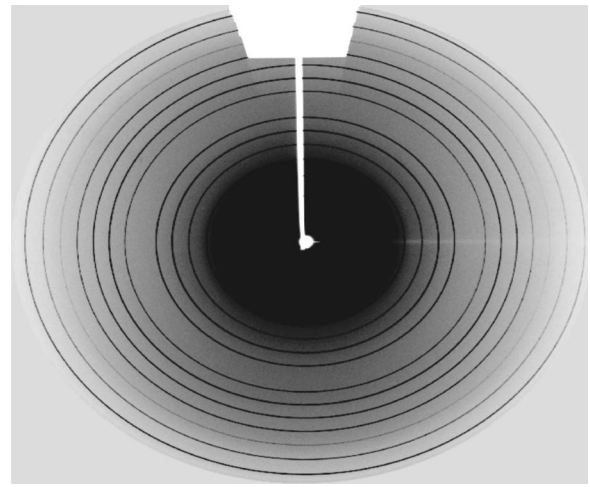


Figure 27. Highly eccentric ellipses: The original image is reduced to a new rectangular dimension to obtain ellipses with high eccentricity.

Ellipses detected from the powder diffraction images have negligible eccentricities. The magnitudes of their eccentricities are so small that these ellipses can be very well approximated to a set of concentric circles. For a circle, the parameter rotation is arbitrary and it becomes irrelevant to describe its geometry. Large scattering in the detected rotations does not necessarily mean huge uncertainties in the major axis lengths for low eccentric ellipse.

Accuracy of estimation of the major axis length and the other parameters cannot be correctly predicted from the rotations of less eccentric ellipses.

B. Ellipse parameters for highly eccentric ellipses

To characterize the quality of the estimated parameters, concentric ellipses of non-negligible eccentricities are made by squeezing the standard image of LaB_6 into a rectangular image of dimension 600×550 (shown in Figure 27).

Reducing to the new dimension results in an elongation along the x direction. Ellipses so obtained have recognizable eccentricities and nearly zero rotation. Parameters detected by the algorithm for this rectangular image are listed in Table V.

Axis lengths for the ellipses in Table V are compared with those calculated from a direct manual method. In the manual method, two lines intersecting at the center of the ellipses and parallel to the coordinate axes are approximated to major and minor axes of all the ellipses.

Axis lengths of individual ellipses are calculated from the mean ellipse positions along the intensity profiles of these lines. Rotations of all the ellipses are approximated to zero. Manually determined parameters are listed in Table VI.

C. Inferences from the parameters of highly eccentric ellipses

Axis lengths of most of the ellipses, extracted from algorithm (Table IV), are found to agree with those calculated by the manual method (Table V). Rotations of smaller radii ellipses are estimated with good precision (Table IV). The magnitudes of rotations for these ellipses (in the order of 4 pixels) are close to the assumed value of rotation (zero) for

TABLE V. The detected parameters for highly eccentricity ellipses: The parameters detected for a rectangular image of LaB_6 are listed. The axes lengths are in pixels and the rotation in degrees. The parameters of first four ellipses are precisely determined. The last four ellipses are imprecisely extracted (in **bold**).

Ellipses	Parameters		
	Major-axis length (<i>a</i>) (pixels)	Minor-axis length (<i>b</i>) (pixels)	Rotation (α) (deg)
1	57.177	52.000	4.514
2	82.718	75.100	4.159
3	102.705	94.000	3.629
4	120.836	111.000	4.271
5	141.796	138.400	83.83
6	150.519	137.000	147.894
7	191.818	171.600	53.907
8	207.515	185.900	127.560

this data. High precision and accuracy of the rotation of the inner ellipses account for the reliable estimation of parameters by this algorithm.

However, we find a large scattering in the rotation for ellipses of large radii. Scattering in the rotation of large ellipses is the result of the uncertainties in major axis detection caused by the occluded ellipses. This can easily be recognized by analyzing the edges of higher radii ellipses.

Continuity of the edges and completeness of the ellipses are important criteria for choosing the best suited ellipse for parameter estimation.

D. Selection criteria for the best rotation and tilt

In powder diffraction images, the ellipses of smaller radii have thick and continuous edges. Such ellipses are preferred for the good performance of the algorithm. Nevertheless the edge pixels of these ellipses are so dense that any parameter estimated using them lacks desired accuracy.

Ellipses with large radii have good resolution with the limitation in their discontinuous edges. The best estimate of rotation is chosen from a trade-off between the resolution of the ellipses and the continuity of their edges.

TABLE VI. Manually determined parameters: The parameters determined by the direct manual method are listed. The rotation is approximated to 0° .

Ellipses	Parameters	
	Major-axis length (<i>a</i>) (pixels)	Minor-axis length (<i>b</i>) (pixels)
1	56.619	52.019
2	81.939	75.021
3	102.165	93.988
4	120.674	110.961
5	137.700	126.690
6	154.096	142.004
7	186.276	171.651
8	202.643	186.755
9	219.036	201.945

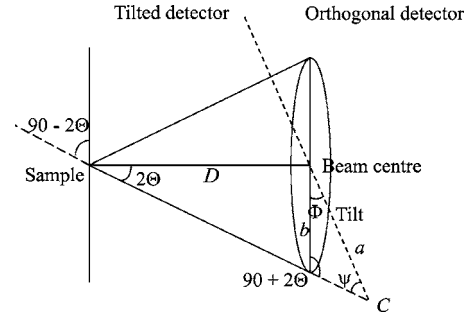


Figure 28. Detector tilt: The pictorial relation between the detector tilt and the parameters of the ellipse.

Continuity of the ellipse edges are measured by an azimuthal scan of the binary image. The routine that makes the initial estimates of axis lengths is used for this purpose. Fifty radial wedges with a step width of 7.2° are used to search the distance peaks representing the ellipses. Distances along the wedges are interpolated to get the distance-intensity profile along radial lines (Figure 18).

For a complete azimuthal scan, the radial distance arrays corresponding to different ellipses are calculated and stored. Each array is expected to hold 50 radii (equal to the number of wedges) of the ellipses in 50 azimuth directions. The distance arrays representing partly occluded ellipses will not contain all the 50 radii.

Experimentally, the arrays with radii elements greater than 90% of the number of wedges have proven to maintain the accuracy of the axis lengths. The arrays meeting these conditions are selected. From the selected arrays, the one with largest radii represents the best ellipse with respect to resolution and continuous contours.

Parameters *a*, *b* and the rotation extracted from this best ellipse are used for the least squares optimization. The tilt of the detector is calculated from the ratio of the axis lengths of this ellipse.

E. Calculation of detector tilt from the parameters

Detector tilt is computed from the parameters of the best resolved and most continuous ellipses formed on the detector. The intersection of a Debye-Scherrer cone on a detector plane is displayed in Figure 28.

A circle of radius *l* is described on the detector plane, for an orthogonal detector intersection. For a tilted detector the radius vector *l* shrinks to the semi-latus rectum of the ellipse formed. The magnitude of the detector tilt is given by

$$\text{Tilt: } \Phi(a, b) = (90^\circ - 2\Theta - \Psi), \quad (11)$$

where ψ is the incident angle and *l* is the semi-latus rectum of the ellipse:

$$\Psi = \arcsin\left(\frac{l \sin(90^\circ + 2\Theta)}{a}\right), \quad (12)$$

$$l = \frac{b^2}{a}.$$

a, *b* are the major and minor axis lengths of the ellipse, and 2Θ is the opening angle of Debye-Scherrer cone.

Equations (11) and (12) are used to calculate the detector alignment in terms of the eccentricity of the ellipse.

F. Least squares refinement of the parameters

The detected parameters (beam-center, tilt, rotation) and the experimental parameters (sample distance D , wavelength λ) are refined using the Levenberg-Marquardt least squares algorithm (William *et al.*, 2002). Parameters are refined by an iterative nonlinear fit of the alignment parameters against the observed ellipse positions by minimizing the difference in their square of deviations (χ^2).

The diffraction angles, as a function of detected parameters, are calculated using Eq. (6). Using the Bragg equation [Eq. (1)] and the experimental wavelength, the Θ values corresponding to half the cone opening angle are computed.

Calculated d spacings are supplied as a dependent input variable (Y') to the algorithm. By supplying d spacings as the dependent variable rather than 2Θ , the refinement of radiation wavelength is made possible. The function of the dependent variable is given by

$$Y'_i = f(X_i, P_j), \quad (13)$$

where X_i are the independent variables representing the pixel coordinates of the ellipses and P_j is the array of detected parameters.

The standard d spacings obtained for the sample (see https://srms.nist.gov/tables/view_table.cfm?table=209-1.htm) are given as the theoretical model to this algorithm:

$$Y_i = f(Y_1, Y_2, \dots, Y_i). \quad (14)$$

Y_i are polynomials representing an array of standard d spacings.

The algorithm establishes a criterion for minimizing the discrepancies between Eqs. (13) and (14) and optimizes the estimates of the parameters. The chi-square function for the observed and true values of d spacings is given by

$$\chi^2 = \sum_i \left(\frac{1}{\sigma^2} [Y'_i(X_i, P_j) - Y_i]^2 \right). \quad (15)$$

The best set of model parameters P that minimizes the χ^2 in Eq. (15) is computed by the algorithm.

The minimum of Eq. (15) is

$$\frac{\partial}{\partial P}(\chi^2) = \frac{\partial}{\partial P} \left(\frac{1}{\sigma^2} \sum_i [Y'_i(X_i, P_j) - Y_i]^2 \right) = 0, \quad (16)$$

where P is an array of detected parameters.

G. Determination of independent variables

The independent variables X_i correspond to the pixel coordinates of ellipses in the detector plane. They are determined using the peaks obtained in an azimuthal scan of the original data.

For good statistics, about 50 wedge-interpolated radial lines are used to scan the full image. Distance-intensity profiles for all 50 lines are obtained (one of them is shown in Figure 29). Peak distances from the center represent the positions of the ellipses. Peak positions are calculated by fitting a Gaussian function to the peaks. It is important to measure

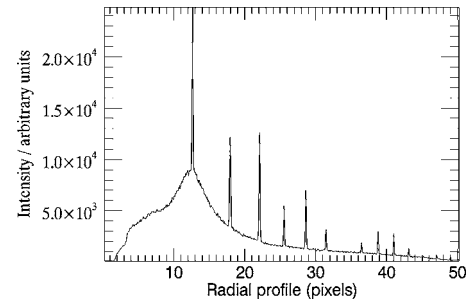


Figure 29. Radial distance-intensity profile of original image: The peaks represent the high intensity pixels of the ellipses. The positions of these peaks are the independent variables required by the least squares fit algorithm.

the peak positions with high accuracy since we assume (Bevington, 1969) that the independent variables (X_i) have negligible uncertainty when compared to the dependent variables (Y_i).

Peak positions (r_i) and the azimuth (β) obtained from the scan are converted into Cartesian form (x, y). They are supplied to the fit function along with Y_i as the input variables.

H. Comparison of estimated parameters and refined parameters

The crystallographic ellipse parameters estimated for the image of LaB_6 are compared with the optimized parameters obtained after a least squares fit in Table VII. The ellipses detected from the estimates are superimposed on the original image. The excellent coincidence of the estimated ellipses and the refined ellipses are shown in Figure 30. The inner ellipses obtained from the estimates of the parameters fit well with original ellipses in the image. After the refinement, all ellipses are superimposed exactly over the original ellipses.

VII. APPLICATION OF “CALIBRATION PROGRAM” TO AgN_3 SAMPLE

A high temperature powder diffraction experiment of AgN_3 (Schmidt *et al.*, 2007) using LaB_6 as a standard sample is calibrated with the presented algorithm. The ellipses detected by the algorithm are superimposed on the original image in Figure 30(b). The refined ellipse parameters and the experimental parameters for this sample are listed in Table

TABLE VII. Estimated parameters and refined parameters: The comparison between the estimated parameters and the refined parameters.

Parameters	Estimated parameters	Refined parameters
x center (pixels)	1162.985	1163.992
y center (pixels)	1144.863	1145.841
Rotation (deg)	99.970	204.255
Tilt (deg)	0.2177	0.1742
Wavelength (nm)	0.09313 ^a	0.09215
Sample distance (m)	1.42998 ^a	1.44906

^aExperimental parameter

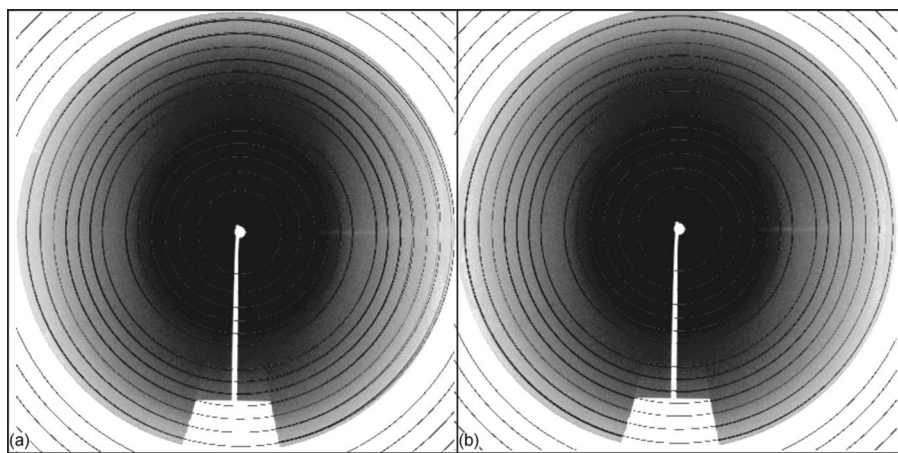


Figure 30. Estimated and refined ellipses: Comparison between the ellipses detected from the estimates (a) and that detected from the refined parameters (b) is shown in terms of their projection on original image. The superimposed rings denote the detected ellipses.

VII (last column). Intensity versus diffraction angle (2θ) for AgN_3 is obtained by integrating the image along the detected ellipses (Figure 31).

A comparison between the integrated powder pattern obtained from “Calibration” and that from FIT2D (Hammersley *et al.*, 1996) is made in Figures 31 and 32. As can be seen from the comparison, all characteristics of the peaks (position, width, and intensity) are affected by erroneous calibration in data obtained from FIT2D (Figure 32). Immediately visible are splitting effects and shifts, both showing a strong angular dependency.

Manual calibration with FIT2D has been carried out by several users, leading to different results with different aberrations. In FIT2D, the beam center is calculated by the optimization of the coordinates of an inner ring of the image used. The tilt angle is calculated from a set of arbitrary points selected by the user along one of the ellipse contours. The source of uncertainty in the parameter estimation arises from the incorrect distinction between ellipses of low eccentricities and circles. An inaccurate initial estimation of the parameters causes the splitting and broadening effects in Figure 32 because of a weakly converging refinement.

The diffraction peaks obtained using the “Calibration” program (Figure 31) are well defined, not showing any splitting or broadening effects. The automated methods in the program are designed to differentiate between ellipses of low eccentricities and circles.

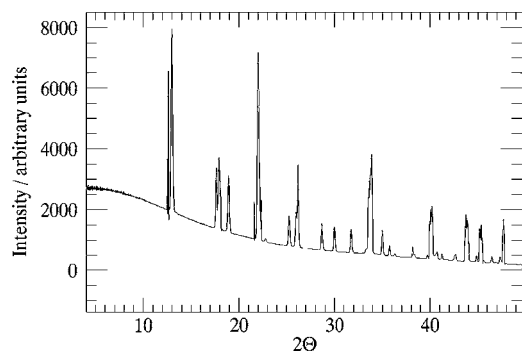


Figure 31. Diffraction pattern from “Calibration”: $I(2\theta)$ histogram of AgN_3 integrated along the ellipses detected by the automated software “Calibration.”

VIII. CONCLUSION

When comparing to existing methods, the diffraction angle data obtained from the algorithm presented are more reliable and better suited for crystal structure determination and Rietveld refinement. The global algorithms used for the estimation of different parameters are capable of distinguishing low eccentric ellipses from circles, thereby producing high quality one-dimensional integrated data. A sensible characterization of ellipses of low eccentricity is made possible with the aid of the global algorithms like the Hough transformation and pattern recognition methods implemented in the program.

Most of the used algorithms are optimized for fast computation and low memory usage. The “Calibration” program is designed and constructed in an object oriented fashion, allowing easy expansion of the modules for future applications. The developed graphical user interfaces are interactive, user friendly, and have minimum manual interaction.

The integration program can further be extended for texture analysis (Wessels *et al.*, 1999) of the diffracting crystallites. Extracted spatial orientation of the crystals can serve as additional information useful for crystal structure determination.

Among others, the masking of high intensity outliers is important for images lacking statistical averaging. Refined

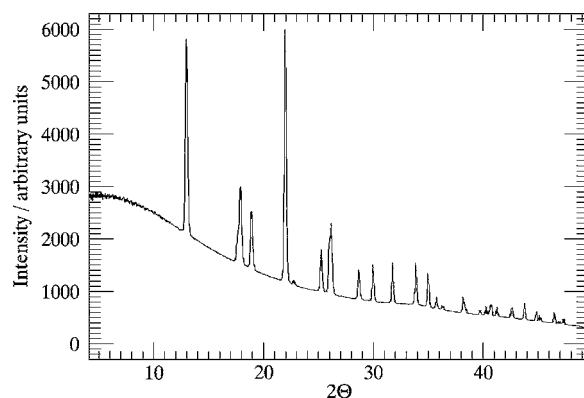


Figure 32. Diffraction pattern from FIT2D: $I(2\theta)$ histogram of AgN_3 obtained from the software FIT 2D (Hammersley *et al.*, 1996) after an imperfect manual calibration of LaB_6 data.

ellipse parameters are the prerequisite for an efficient fractile masking of these experimental artefacts. For a long term view, phase diagrams will be automatically evaluated from *in situ* X-ray powder diffraction data using area detectors. We regard our program as one of the first steps in achieving this goal.

- Bennett, N., Burrige, R., and Saito, N. (1999). "A method to detect and characterize ellipses using Hough transform," IEEE Trans. Pattern Anal. Mach. Intell. **21**, 652–657.
- Bevington, R. P. (1969). *Data Reduction and Error Analysis for the Physical Sciences* (McGraw-Hill, New York).
- Cervellino, A., Giannini, C., Guagliardi, A., and Ladisa, M. (2006). "Folding a two-dimensional powder diffraction image into a one-dimensional scan: a new procedure," J. Appl. Crystallogr. **39**, 745–748.
- Chellali, R. and Fremont, V. (2003). "Ellipse detection using Hough Transform," *13th International Conference on Artificial Reality and Telexistence*, Tokyo, Japan.
- Dammer, C., Leleux, P., Villers, D., and Dosiere, M. (1997). "Use of Hough Transform to determine the center of digitized X-ray diffraction patterns," Nucl. Instrum. Methods Phys. Res. B **132**, 214–220.
- Feng, L. and Fainman, Y. (1992). "Detection of a general ellipse by an optical Hough transform," Appl. Opt. **31**, 3259–3262.
- Fisker, R., Poulson, H. F., Schou, J., Carstensen, J. M., and Garbe, S. (1998). "Use of images-processing tools for texture analysis of high-energy synchrotron data," J. Appl. Crystallogr. **31**, 647–653.
- Fung, P. F., Lee, W. S., and King, I. (1996). "Randomized generalized Hough Transform for 2-D grayscale object detection," *Proceedings of International Conference on Pattern Recognition*, Vienna, Austria.
- Hammersley, A. P., Svensson, S. O., Hanfland, M., Fitch, A. N., and Häusermann, D. (1996). "Two-dimensional detector software: from real detector to idealized image or two-theta scan," High Press. Res. **14**, 235–248.
- Hinrichsen, B., Dinnebier, R. E., Rajiv, P., Hanfland, M., Grzechnik, A., and Jansen, M. (2006). "Advances in data reduction of high pressure X-ray powder diffraction data from two dimensional detectors: A case study of Schafarzikite (FeSb₂O₄)," J. Phys.: Condens. Matter **18**, S1021–S1037.
- Hough, P. V. C. (1962). "Methods and Means for Recognizing Complex Patterns," U.S. Patent No. 3,069,654.
- Kanatani, K. and Ohta, N. (2001). "Automatic detection of circular objects by ellipse growing," Mem. Faculty Eng. Okayama Univ. **36**, 107–116.
- Lei, Y. and Wong, K. C. (1999). "Ellipse detection based on symmetry," Pattern Recogn. Lett. **20**, 41–47.
- Norby, P. (1997). "Synchrotron powder diffraction using imaging plates: crystal structure determination and Rietveld Refinement," J. Appl. Crystallogr. **30**, 21–30.
- Pecharsky, V. K. and Zavalij, P. Y. (2003). *Fundamentals of Powder Diffraction and Structural Characterization of Materials* (Springer, New York).
- Schmidt, C., Dinnebier, R. E., Wedig, U., and Jansen, M. (2007). "Crystal structure and chemical bonding of the high temperature phase of AgN₃," Inorg. Chem. **46**(3), 907–916.
- Schreckenberger, M. and Joswig, M. (1993). "Kompensation von Rippen-schatten in digitalen Thorax-Röntgenbildern" in *Mustererkennung 1993*, edited by S. J. Pöpl and H. Handels (Springer-Verlag, Berlin), pp. 522–527.
- Wessels, T., Baerlocher, C., and McCusker, L. B. (1999). "Single-crystal-like diffraction data from polycrystalline materials," Science **284**, 477–479.
- William, H. P., Teukolsky, S. A., Vetterling, W. T., and Flannery, B. P. (2002). *Numerical Recipes in C: The Art of Scientific Computing*, 2nd ed. (Cambridge U. P., Cambridge).
- Wunschel, M. (2003). "X-ray Powder Diffraction Studies at non-Ambient Conditions on the Compounds In_xNb₃Te₄ (x=0,0.54) and Si[C(CH₃)₃]_n[Si(CH₃)₃]_{4-n} (n=0,1,2)," Ph.D. thesis, Universität Bayreuth, Germany, pp. 19–44.